2

CONF-840616--21

UCRL-90879
PREPRINT

RECENT EXPERIMENTAL PROGRESS IN THE TMX-U THERMAL BARRIER TANDEM MIRROR EXPERIMENT

W. C. Turner, S. L. Allen, T. A. Casper, J. F. Clauser, F. H. Coensgen, D. L. Correll, W. F. Cummins, C. C. Damm, J. H. Foote, R. K. Goodman, D. P. Grubb, D. N. Hill, E. B. Hooper, Jr., R. S. Hornady, A. L. Hunt, R. G. Kerr, G. W. Leppelmeier, J. Marilleau, A. W. Molvik, W. E. Nexsen, W. L. Pickles, G. D. Porter, P. Poulsen, E. H. Silver, T. C. Simonen, B. W. Stallard, W. L. Hsu, T. L. Yu, J. D. Barter, T. Christensen, G. Dimonte, T. W. Romesser, R. F. Ellis, R. A. James, C. J. Lasnier, L. V. Berzins, M. R. Carter, C. A. Clower, B. H. Failor, S. Falabella, M. Flammer, and T. Nash

MASTER

This paper was prepared for submittal to the Proceedings of the 1984 International Conference on Plasma Physics, Lausanne, Switzerland, June 27-July 3, 1984.

June 22, 1984

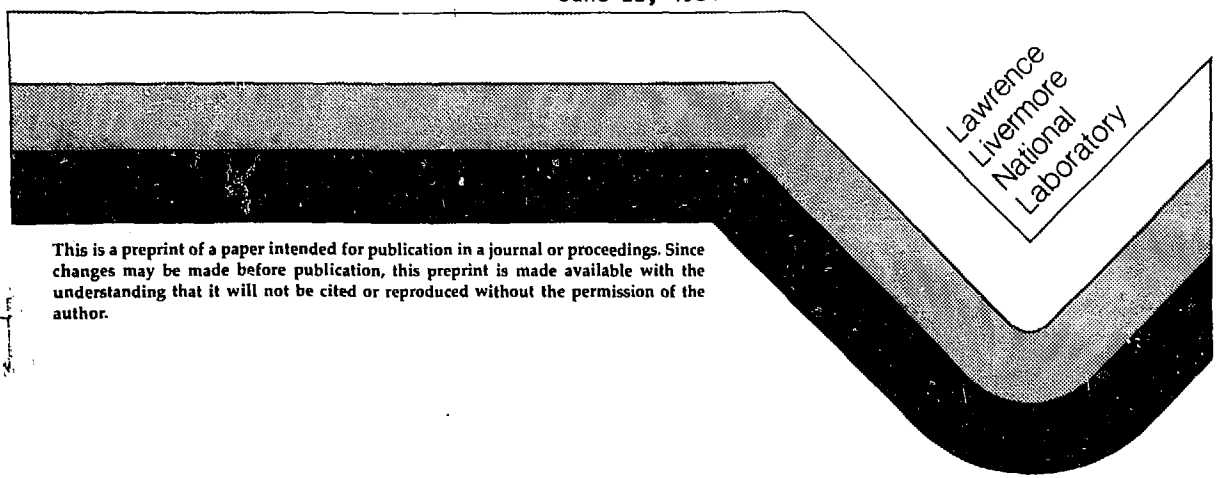

UCRL--90879

DE84 015605

RECENT EXPERIMENTAL PROGRESS IN THE TMX-U THERMAL BARRIER TANDEM MIRROR EXPERIMENT*

W. C. Turner, S. L. Allen, T. A. Casper, J. F. Clauser, F. H. Coensgen
D. L. Correll, W. F. Cummins, C. C. Damm, J. H. Foote, R. K. Goodman
D. P. Grubb, D. N. Hill, E. B. Hooper, Jr., R. S. Hornady, A. L. Hunt
R. G. Kerr, G. W. Leppelmeier, J. Marilleau, A. W. Molvik, W. E. Nexsen,
W. L. Pickles, G. D. Porter, P. Poulsen, E. H. Silver,
T. C. Simonen, and B. W. Stallard
Lawrence Livermore National Laboratory, University of California
Livermore, CA 94550

W. L. Hsu
Sandia National Laboratory, Livermore, CA 94550

T. L. Yu
Johns Hopkins University, Baltimore, MD 21218

J. D. Barter, T. Christensen, G. Dimonte, and T. W. Romesser
TRW Corporation, Redondo Beach, CA 90278

R. F. Ellis, R. A. James, and C. J. Lasnier
University of Maryland, College Park, MD 20742

L. V. Berzins, M. R. Carter, C. A. Clower, B. H. Failor.
S. Falabella, M. Flammer, and T. Nash
University of California-Davis, Livermore, CA 94550

Abstract. -- Recent experiments on the TMX-U thermal barrier device at LLNL have achieved the end plugging of axial ion losses up to a central cell density of $n_c = 2 \times 10^{12}$ cm. During these tests, the axial potential profile characteristic of a thermal barrier has been measured experimentally, indicating an ion-confining potential greater than 1.5 kV and a potential

depression of 0.45 kV in the barrier region. The average beta of hot electrons in the thermal barrier has been increased to 15% and appears limited only by classical scattering and ECRH pulse duration. Furthermore, deuterium ions in the central cell have been heated with ICRF to an average energy of 1.5 keV, with a heating efficiency of 40%. During strong end plugging, the axial ion confinement time reached 50 to 100 ms while the nonambipolar radial ion confinement time was 5 to 15 ms--independent of end plugging. Radial ion confinement time exceeding 100 ms has been attained on shots without end plugging. Plates, floated electrically on the end walls, have increased the radial ion confinement time by a factor of 1.8. Further improvement in the central cell density during end plugging can be expected by increasing the ICRF, improving the central cell vacuum conditions and beam heating efficiency, and increasing the radial extent of the potential control plates on the end walls.

*Work performed under the auspices of the U.S. Department of Energy by the Lawrence Livermore National Laboratory under contract number W-7405-ENG-48.

1. Introduction. -- The Tandem Mirror Experiment-Upgrade (TMX-U) at Lawrence Livermore National Laboratory (LLNL) is the first thermal barrier tandem mirror to operate. Our recent experimental results demonstrate the formation of microstable sloshing-ion distributions [1], end plugging with a density larger in the central cell than the end plug [2], and measurement of an axial potential profile in the thermal barrier [3]. Additional work has shown the continued increase of hot electron beta (up to $\langle\beta\rangle = 1/2\,\hat{\beta} = 0.15$) in the barrier, with increasing power capability of the electron-cyclotron resonant heating (ECRH) wave-launching structure [4], heating of the central cell ions by ion-cyclotron resonant frequency (ICRF) [5], and decreased radial ion transport with end wall potential control [6]. In this paper we review this work and point out the new directions of our next experiments.

A schematic of the TMX-U machine is shown in Fig. 1, and pertinent machine parameters are listed in TABLE I. Specifically, the magnetic field configuration consists of a solenoidal central cell terminated at each end by a single quadrupole mirror cell that performs the dual role of providing a thermal barrier potential profile for axial confinement as well as both high pressure and good curvature for magnetohydrodynamic (MHD) stability.

Neutral beams, injected in the end plugs at 47^{0} to the magnetic field, form sloshing-ion distributions and charge-exchange pump trapped ions out of the thermal barrier. In the central cell, neutral beam injection heats potentially confined ions and electrons. In each end plug, two 28-GHz gyrotrons heat electrons near the second harmonic resonance at the bottom of the magnetic well and at the fundamental resonance (ω_{ce}) between the bottom of the well and the outside mirror. Central cell ions are heated by two ICRF antennas. The plasma is fueled by injecting gas in the central cell transition regions.

The axial potential profile can be biased relative to ground potential with electrodes on the end walls. A Ti-gettered wall near 350 K separates the plasma from the magnet structure illustrated in Fig. 1. Not shown in Fig. 1 are two, co-axial cylinders of Ti-gettered, LN-cooled cryopanels that lie between the magnets and outer vacuum wall; these cryopanels provide two regions for differentially pumping gas from the beam arc chambers.

Calculated axial profiles of potential and particle densities are depicted in Fig. 2 for the thermal barrier end plugs of TMX-U [7]. Note the three distinct types of electron and ion distributions. As shown, hot,

TABLE I. Summary of pertinent machine parameters for TMX-U.

Magnets	
End plug:	
Midplane field (T)	0.5
Mirror ratio	4:1
Length (m)	3
Central cell:	
Midplane field (T)	0.3
Length (m)	8
Neutral beams	
Average injection energy (keV)	10
Injected sloshing-beam current (47^{o})/plug (A)	80
Injected central cell current (A)	145
Pulse duration (ms)	75
Electron-cyclotron resonant heating	
Gyrotrons	4
Frequency (GHz)	28
Transmitted power (kW)	600
Pulse duration (ms)	50
Ion-cyclotron resonant heating	
Transmitters	2
Frequency (MHz)	2 to 5
Transmitted power (kW)	200
Pulse duration	dc
Vacuum	
Volume (ℓ)	2.12×10^{5}
Machine length (m)	22
LN cryopanel area (m^2)	540
Ti gettering/shot (gms)	20
Pumping speed (ℓ/s)	23×10^{6}
Base pressure (T)	1×10^{-8}

mirror-confined electrons are produced at the bottom of the magnetic well by second-harmonic ECRH and provide the dip in potential at the thermal barrier (b). The magnitude of the potential dip ϕ_b between the central cell and thermal barrier is a sensitive function of the fraction of hot electrons at the thermal barrier. Specifically,

$$\frac{\phi_b}{T_{ec}} = \ln \frac{n_c}{n_b\,(1 - f_{e\text{-}hot})} \quad , \tag{1}$$

where T_{ec} is the central cell electron temperature, n_c and n_b are the electron densities in the central cell and thermal barrier, respectively, and $f_{e\text{-}hot}$ is the hot electron fraction in the thermal barrier. The outer potential peak (p)--also shown in Fig. 2--is formed by both the sloshing-ion distribution and by electron heating with fundamental ECRH. The warm electrons in the potential peak are confined by the potential and thermally insulated from central cell electrons by the potential dip ϕ_b. Heating these electrons increases their loss rate and thus the magnitude of the potential peak until their loss balances the loss of ions.

Passing ions from the central cell turn on the inboard side of the outer potential peak, whereas passing electrons from the central cell turn on the thermal barrier and outboard side of the outer potential peak. In addition, a class of potential trapped ions exists in the thermal barrier that must be removed by charge-exchange pumping with neutral beams. With strong ECRH heating, the potentially trapped electrons can be expected to be distorted from a Maxwellian distribution [8,9]. In this strong ECRH limit and for mirror ratios appropriate to TMX-U, the predicted ion-confining potential ϕ_c between the outer peak and central cell can be approximated by:

$$\frac{\phi_c}{T_{ec}} = \frac{2}{3}\left(\frac{n_p}{n^*_b}\right)^{2/3}\left(\frac{n_c}{n^*_b}\right)^{1/5} - \ln\left(\frac{n_c}{n^*_b}\right) \quad , \tag{2}$$

where n_p is the plasma density at the potential peak and n^*_b is the density of passing electrons at the barrier. Because $n^*_b = n_b\,(1 - f_{e\text{-}hot})$, ϕ_c is also a sensitive function of the thermal barrier hot electron fraction.

2. **Thermal barrier startup.** -- In TMX-U, thermal barrier startup proceeds in three stages: (1) plasma formation and hot electron buildup at low density ($\sim 5 \times 10^{11}$ cm^{-3}); (2) sloshing ion injection and potential

formation; and (3) central cell density buildup. An example of this sequence is shown in Fig. 3, beginning with ECRH breakdown and ionization of the deuterium gas.

Initially, the density must be low because the absorbed ECRH power satisfies $P_{ECRH} \sim n^2/(T_e)1/2$ and the low initial temperature requires low density to generate the hot mirror-confined electrons. Formation of the outer potential peak is inferred from Fig. 3 when the sloshing beams turn on and the axial end losses measured by Faraday cup arrays sharply decrease. The negative currents recorded on the Faraday cups are caused by electrons with energies greater than the suppressor grid bias (-2 kV). In the east end plug, the ion end loss current increases again when the sloshing beams are turned off. However, the beam duration is longer in the west end plug, and suppression of ion end losses continues there until the ECRH is turned off.

From this, we can infer the necessity of sloshing-ion injection and ECRH for potential confinement. Once potential confinement is established, the maximum central cell density is determined by the equilibrium between the neutral beam pumping rate and the collisional trapping rate of the thermal barrier (that is, $n_c^2/T_{ic}^{3/2}$, where n_c is the central cell density and T_{ic} is the central cell ion temperature). Because of the $n_c^2/T_{ic}^{3/2}$ dependence of the trapping rate, heating the central cell ions must be done simultaneously with increasing the central cell density [10]. During startup at low density--where neutral beam injection heating is inefficient--central cell ions are heated by ICRF.

Impurity concentrations, measured in TMX-U with extreme ultraviolet spectroscopy [11], are very low. Oxygen, nitrogen, and carbon--the most abundant impurities--are typically present at concentrations of 0.9, 0.5, and 0.9%, respectively, in the central cell. These impurities radiate an estimated 4 kW, which is negligible compared to the power input to the plasma. So far, no accumulation of impurties in the end plug thermal barrier region has been noted.

3. **Sloshing ions.** -- Sloshing ions are detected by an angular array of secondary electron emission detectors (SED) that view a common volume at the end plug midplane. A typical sloshing-ion angular distribution [1] is shown in Fig. 4a and the corresponding axial density distribution, obtained by Abel inversion [12], in Fig. 4b. The pitch-angle distribution, peaked near the

47^{0} injection angle, is in reasonable agreement with the Fokker-Planck calculation shown by the solid line.

The sloshing-ion distribution produced in TMX-U has improved microstability over the single cell 2XIIB mirror and the TMX standard tandem mirror. Both 2XIIB and TMX employed 90^{0} beam injection. Neither the Alfven ion-cyclotron (AIC) anisotropy-driven mode observed in TMX [13] nor the strong drift-cyclotron loss cone (DCLC) electrostatic oscillations in 2XIIB [14] that were near the fundamental of the mid-plane ion-cyclotron frequency have yet been observed in TMX-U.

Theoretically, this improved microstability is expected because the reduced anistropy in TMX-U stabilizes the AIC mode whereas warm, potentially trapped ions and passing ions from the central cell stabilize loss-cone modes. Although low-level ion-cyclotron oscillations have been observed in TMX-U at a frequency 1.8 times the plug midplane fundamental, these apparently do not affect confinement. Furthermore, the frequency matches the ion-cyclotron frequency outside the peak of the sloshing-ion density distribution where warm ions could not be electrostatically confined. The oscillations neither propagate to the central cell nor heat the central cell ions escaping through the end plugs, which was characteristic of the AIC mode in TMX [13].

4. Hot **electrons.** -- To achieve the moderate densities (a few $\times 10^{12}$ cm^{-3}) of hot (50 to 150 keV) mirror-trapped electrons required for a thermal barrier and at the same time avoid the production of a low density, runaway electron population, the ECRH system for TMX-U is designed for localized wave fields and high, single-pass, absorption efficiency. We use mode conversion to transform the predominantly TE02 gyrotron radiation to the linearly polarized extraordinary mode.

Early experiments on TMX-U incorporated arrays of fundamental-mode waveguides and horns to produce localized fields, whereas more recent experiments have used overmoded waveguides and polarizing reflectors [4]. Ray-tracing calculations, which predict high, single-pass absorption efficiency, have been verified by spatial profile measurements of $2\omega_{ce}$ transmission through the plasma. We used Fokker-Planck calculations to model hot electron formation and demonstrate that fundamental ECRH acts as a feed for the hot electron population. We also found that cold electrons are efficiently heated to a few kiloelectron volts by absorption of fundamental

ECRH and then further heated to the range of 100 keV by second-harmonic ECRH [15]. Experimentally this is borne out by the increased efficiency of hot electron production when both ω_{ce} and $2\omega_{ce}$ heating are employed--compared to one or the other used alone.

An example of the buildup of hot electron diamagnetism is shown in Fig. 5a. For this shot 75 kW was applied at both ω_{ce} and $2\omega_{ce}$. From the initial rate of increase of diamagnetic energy, an overall heating efficiency of 42% was obtained. The hot electron diamagnetism, which continued to increase for the duration of the ECRH pulse, is consistent with the buildup against classical scattering losses. Thus, from the data in Fig. 5a, an average hot electron beta of $\langle\beta\rangle = 0.15$ can be calculated--the highest hot electron beta achieved. This result is plotted in Fig. 5b for a integrated ECRH power input of 6.3 kJ together with some earlier data at lower power and efficiency.

We measured the hot electron radius by inserting a radial limiter on a succession of shots (Fig. 6a, b). The decreases in both diamagnetism and perpendicular emission detected by a radiometer tuned to $f/f_{ce} = 2.5$ have been fit with a 20-cm parabolic radius. The hot electron length has been determined from the diamagnetism measured with axially displaced diamagnetic loops and from the signal strength received by an axially scanning radiometer. A fit to these data gives a Gaussian e-folding half length of 64 cm. In addition, we detected a hot electron "tail" temperature by observing the bremsstrahlung x-ray emission above 40 keV. This tail temperature typically falls in the range of 75 to 200 keV.

The magnitude of confining potential is expected to depend sensitively on the fraction of hot electrons at the plug midplane. For TMX-U, theory [8] predicts that a ratio of $n_{e\text{-hot}}/n_{total} \simeq 0.8$ is required for a confining potential of $\phi_c > 0$. We measured the hot electron temperature for a series of shots with a radiometer [16] and combined our results with diamagnetism measurements to estimate the hot electron density. The total density was measured with an inferometer. Figure 5c depicts our data: the hot electron density is plotted versus total density for shots which did and did not achieve end plugging of central cell ions. With the exception of a single entry, the data show clearly that end plugging requires a large fraction of hot electrons. In addition, the shots on which end plugging was achieved lie close to the theoretical, minimum-required, hot electron fraction.

Although we observed fluctuations in microwave emission near the

electron-cyclotron frequency to exceed thermal levels, so far these do not seem to degrade hot electron confinement [17]. Total radiated power is typically less than 100 W. Three distinct bands of radiation frequencies have been observed and are consistent with the frequencies expected for anisotropy-driven whistler waves (<13 GHz) [18], the electron cyclotron maser instability (13.5 to 14 GHz) [19], and the upper hybrid loss cone instability (14.3 to 16.5 GHz) [18,20].

5. **Measurements of the thermal barrier potential.** -- Using the experimental technique depicted in Fig. 7, we measured the depression of the thermal barrier potential [3]. The machine operated in a single end plug mode, and both sloshing beams and ECRH heating were applied in the standard manner to create an end-plugging plasma in the west end cell (Fig. 7a). However, only second harmonic ECRH was used in the east end cell for electron heating, and there was no end plugging there. In addition, in the west end cell a diagnostic neutral beam was injected at a small angle (18^{o}) to the magnetic axis.

The diagnostic beam atoms are not magnetically trapped when ionized in the plasma, but stream along magnetic field lines out the east end of the machine. The energy spread of these ions, superimposed on the beam extraction energy, gives a direct measure of the barrier depth ϕ_b along the axial extent sampled by the beam. Three gridded electrostatic analyzers [20] (located at the ends of the machine) were used to measure the potentials. The ion repeller grid for the analyzer labelled ELA1 in Fig. 7b was swept around the energy of the diagnostic beam (the 5-keV third energy component is used), and the resulting energy width of detected ions yields ϕ_b. The analyzers labelled ELA2 and ELA3 were swept through a a lower energy range--from ground to 2.4 keV. Ions detected by these analyzers have a minimum energy ϕ_e (ELA2) or ϕ_p (ELA3), as determined by the decrease in ion current when the ion repeller grid voltage was swept through these values of potential.

Typical results showing the thermal barrier depression are indicated in Fig. 7b with ϕ_e = 0.88 kV, ϕ_b = 0.45 kV, and ϕ_p > 2.4 kV. The peak potential height ϕ_p was not resolved because ions lost out the west end had energies greater than the maximum grid bias of 2.4 kV. Therefore, the central cell ion-confining potential $\phi_c = \phi_p - \phi_c$ exceeds 1.5 kV. A cross-check of these measurements is available because the analyzer detecting

the diagnostic beam ions should "see" a maximum energy ϕ_e above the measured beam extraction voltage. We found that the value of ϕ_e obtained in this way is in agreement with ELA2.

There is additional supporting evidence for a thermal barrier in TMX-U. The central cell density n_c has been observed to exceed end plug density n_p (n_c/n_p ratios up to 2). Also, the electron temperature T_{ep} measured by Thomson-scattering diagnostics at the location of the potential peak showed a trend of exceeding the electron temperature T_{ec} measured in the central cell [22]. Our Thomson-scattering data are shown in Fig. 8 where T_{ec} is plotted versus T_{ep} with lines drawn for the various ratios of T_{ep}/T_{ec}. It should be noted that the Thomson-scattering data at the location of the potential peak show a non-Maxwellian distribution (Fig. 8b) that is qualitatively similar to Monte Carlo calculations of strong electron-cyclotron heating [9] (Fig. 8c). For purposes of plotting the data in Fig. 8a, only the low-energy portion of the Thomson-scattering data is used.

6. **Central cell ion-cyclotron heating.** -- Ion-cyclotron heating is used for bulk heating of the central cell ions, especially during buildup from low density ($n_c \sim 10^{12}cm^{-3}$) where beam trapping efficiency is low [10]. The most recent results have been obtained from a two-loop antenna with a Faraday shield [5]. Each loop subtends a 170^0 arc around the plasma circumference, and the loops are excited in the m=1 configuration. The loop antenna is located at a distance z = 124 cm from the midplane of the central cell. The magnetic field strength at the antenna is B = 3.8 kG whereas the field minimum is B = 3.0 kG at the midplane.

Figure 9 shows an example of central cell ion heating with this antenna. The antenna has been tuned to a frequency of f = 2.48 MHz, which is below the local cyclotron frequency (f/f_{ce} = 0.85) where slow waves are theoretically excited. Initially, the central cell density is $8 \times 10^{11}cm^{-3}$ and then builds up to $2 \times 10^{12}cm^{-3}$ as 75 to 100 kW of ICRF are applied and as gas fueling is increased. The perpendicular ion temperature, determined by plasma diamagnetism, increases to 1.5 keV soon after ICRF is turned on. At the same time the ion temperature of ions escaping axially out the ends of the device increases--from 70 to 140 eV as ICRF is applied--but remains much less than the diamagnetism temperature, indicating strong anisotropy of the heated central cell ions. (The decrease in ion temperature after 55 ms coincides

with turn-off of ECRH power and a presumed increase in electron drag.) After the ICRF is turned off, the diamagnetism decays (with an approximate 3-ms time constant) because of the combined effects of electron drag and charge exchange. This decay rate is less than the ion-ion scattering time to reach the mirror throats (about 10 ms).

Since the first observation of end plugging in TMX-U in February 1983, the central cell density n_c has been steadily increased with vacuum improvements [23] and increased levels of ICRF and ECRH heating power. Figure 10 shows the improved n_c (from 1.5×10^{11} to 2×10^{12} cm^{-3}) as these changes were made. Our ultimate goal is to increase n_c another order of magnitude to $2 \times 10^{13} cm^{-3}$. The recent addition of a second ICRF antenna combined with central cell vacuum improvements and re-orientation of the neutral beam injectors to achieve higher absorption efficiency are expected to take the experiment closer to this goal.

As mentioned earlier in this paper, it is necessary to increase the central cell density and temperature at the same time to avoid excessive collisional trapping of the ions and charge neutralizing warm electrons in the thermal barrier region. These warm particles are characterized by the ratio:

$$g = \frac{n_{pass} + n_{trap}}{n_{pass}} \quad , \tag{3}$$

where n_{pass} is the density of passing ions and n_{trap} is the number of trapped ions in the barrier.

In the present experiment, trapped ions are removed by charge-exchange pumping, with approximately 100 A of neutral beam current injected into the end plugs. Equilibrium between the collisional filling and charge-exchange pumping determines $n_c/T_{ic}^{3/2}$ for each value of g. Figure 11 shows lines of constant $n_c/T_{ic}^{3/2}$ for g = 2, where the thermal barrier is well pumped and for g = ∞, where the thermal barrier is non-existent. Also in Fig. 11 are a number of data points indicating where end plugging was either not achieved or was lost before the sloshing beams and/or fundamental ECRH were turned off. Note that these data points tend to lie above the g = 2 line.

Also shown schematically in Fig. 11 are "islands" where end plugging is either routinely observed or not observed at all in the present experiment. In addition to collisional trapping, cold ions can be trapped in the thermal barrier by both ionization of neutral particles penetrating the plasma, and by

charge exchange of the sloshing or passing ions with neutrals; this may account for some of the scattering of data points in Fig. 11. In any case, we can infer from Fig. 11 that there are not large departures from Coulomb processes as would occur with the possible microinstabilities [24] associated with the thermal barrier configuration. Assuming this to be the case, Fig. 11 indicates that the path to achieving n_c in the range of $10^{13}cm^{-3}$ lies in increasing the temperature of passing ions (and, therefore, the temperature of central cell ions reaching the end wall) to 1 keV, using both ICRF and neutral-beam-injection heating.

7. **Central cell ion confinement and potential control.** -- During the axial end plugging illustrated in Fig. 3, the ion end losses are strongly suppressed. The fact that the "ion" end loss currents in Fig. 3 are negative during plugging is caused by electrons with energies exceeding the electron repeller voltage (-2 kV) of the Faraday cup detectors. Although small, the ion end loss current is finite during plugging and has been measured with the same end loss analyzers used for the axial potential measurements depicted in Fig. 7. Here the repetitively swept ion repeller grid allows the ion current to be resolved against the electron background. For $n_c \simeq 7 \times 10^{11}cm^{-3}$, the axial ion confinement time is in the range of $\tau_{\parallel}$ = 50 to 100 ms during strong plugging and about an order-of-magnitude less--2 to 20 ms--without plugging. By contrast, the radial ion confinement time, which is insensitive to the presence or absence of end plugging in the present experiments, is $\tau_{\perp}$ = 5 to 15 ms. This radial confinement time is determined by an array of net current collectors on the end walls. Negative currents, implying an axial current of electrons exceeding that of ions, are measured and an equal charge balancing radial current of ions is used to calculate $\tau_{\perp}$.

Figure 12 shows the experimental scaling of $\tau_{\perp}$ with ϕ_e where ϕ_e is the potential of the central cell plasma relative to ground. (Note that ϕ_e is measured without end plugging by using an end-loss analyzer.) For the data in Fig. 12 we measured the net electric current to the grounded end walls to calculate $\tau_{\perp}$ for the central cell plasma ions inside a radius of r_c = 12.9 cm (where $\tau_{\perp}$ equals the number of central cell ions with an $r \leq r_c$/net axial current). Because $\tau_{\perp}$ is not observed to change with end plugging, the data in Fig. 12 have been obtained over wide ranges of $\tau_{\perp}$ and ϕ_e without end plugging when $50 < T_e < 80$ eV. In this way we

could determine ϕ_e from the energy spectrum of axially escaping ions.

Above ϕ_e = 150 V, $\tau_\perp$ decreases as ϕ_e^{-2}, whereas at lower values of ϕ_e, $\tau_\perp$ is roughly constant and equal to 0.1 to 0.2 s. The region of ϕ_e^{-2} scaling includes the resonance between the ion axial bounce and azimuthal E x B drift motions, where resonant transport theory predicts a general increase in radial transport [25]. Initial estimates indicate that the measured transport increases more rapidly than predicted; near resonance the theoretical calculations of $\tau_\perp$ overlap the experimental data, whereas at higher potential the theoretical predictions are roughly a factor of 10 greater than experimental data [26]. Overall, our experiments show the importance of avoiding tandem mirror operation at excessively high values of potential relative to the ion and electron temperatures (as predicted by theory).

Although ECRH was on while the data in Fig. 12 were recorded, information has been obtained very recently during beam injection with the ECRH turned off. For this testing, ϕ_e = 600 V and $\tau_\perp$ = 5 to 10 ms, again falling close to the ϕ_e^{-2} scaling shown in Fig. 12. This strongly suggests that it is the magnitude of the ϕ_e, or equivalently the radial electric field in the central cell, that determines radial ion transport.

Because of its nonambipolar nature and relation to central cell potential, radial ion transport should be amenable to control with conducting plates on the end walls of the machine; these may either be electrically floated or biased. Preliminary experiments with such plates have increased the ion confinement time [6]. Specifically, nonambipolar transport in tandem mirror devices with nonaxisymmetric magnetic fields, as in the quadrupole transitions and end plugs of TMX-U, can arise from the resonance between the axial bounce and azimuthal E x B drift frequencies of the central cell ions [25]. Negatively biased plates on the end wall can transfer the radial electric field from the transition region to the end fan region outside the confined plasma, and thus reduce the azimuthal E X B drift frequency and increase the ion energy threshold required for resonance.

Results from our first experiments to utilize potential control on TMX-U are shown in Fig. 13; a sketch of the experimental arrangement is included. In this arrangement (Fig. 13a), two end wall electrodes at each end of the device may be electrically floated and the voltage measured, or switched to

ground and the current measured. The inner electrode is an elliptical disc (ellipicity = 5.0) that maps to a circle with radius r_c = 9.8 cm in the central cell, whereas the outer electrode is an elliptical disc that extends to r_c = 12.9 cm. The magnetic field strength at the plates is 150 G. Because the actual plasma extends beyond r_c = 20 cm, these plates can only influence the plasma core.

In Fig. 13b, the end plates are floating (-1200 V on the inner plates) until t = 35 ms when they are switched to ground. Since the plasma sources are fixed, the fact that the exponential build-up time decreases from 7.1 to 0.0 ms as the plates are shorted is clear evidence of superior confinement while the plates are floating. For this shot, the axial and radial ion currents immediately after the plates are shorted are $I_{\parallel}$ (35+) = 2 A and $I_{\perp}$ (35+) = 6 A, respectively. The total number of plasma ions is 2×10^{17} at t = 35 ms, giving an axial confinement time $\tau_{\parallel}$ (35+) of 17 ms, a radial confinement time $\tau_{\perp}$ (35+) of 5.6 ms, and a total confinement time of $\tau_{\perp}$(35+) = 4.2 ms. The radial confinement time prior to shorting the plates is then given by:

$$\frac{1}{\tau_{\perp}\ (35-)} = \frac{1}{\tau\ (35+)} + \frac{1}{N}\frac{dN}{dt}\bigg|_{35+} - \frac{1}{N}\frac{dN}{dt}\bigg|_{35-}$$

$$= \frac{1}{10.3\ \text{ms}} \quad . \tag{4}$$

Radial confinement increases with the plates floating by a ratio of 10.3/5.6 = 1.8. Additional evidence of improved radial confinement is the narrower radial density profile before these plates are shorted. This is determined by the ratio R of line densities measured through chords at r = 0 and r = 13 cm. As shown in Fig. 13c this ratio decreases at 35 ms when the plates are shorted. For the particular shot shown in Fig. 13, end plugging failed nearly simultaneously with shorting of the end plates. However, it is known from other shots taken in the same run that the failure of the end plugging did not strongly change the density buildup rate because the radial confinement time was independent of the end plugging and characteristically much shorter than the axial confinement time during plugging.

Additional data taken by separately grounding the inner and outer electrodes has shown that the negative axial current observed with the shorted plates is not caused by radially inward electron current. Also, suppressing

the negative current corresponds to a decrease in the outward radial ion current rather than an increase in the outward radial electron current.

These initial end plate experiments have given confidence that the gross central cell plasma parameters can be controlled by changing the electrical boundary conditions at the end walls. The negative floating potentials reached by the plates are similar in magnitude to the positive central cell potential observed with grounded plates, with a maximum value of 1400 V reached so far. Furthermore, these experiments have clearly demonstrated that small magnetic field line errors, which exist at the 1-cm level end-to-end, do not result in effectively grounding the plates. To extend the results obtained so far, the number of plate elements has been increased from two to five on each end, and the central cell radius mapped to the plates has been increased from 12.9 to 19.5 cm.

8. **Summary.** -- Thermal barrier end-plugging experiments have been conducted on TMX-U up to a central cell density $n_c = 2 \times 10^{12} cm^{-3}$. Hot electrons have been created in the thermal barrier region with an average beta up to 15% and a 42% heating efficiency. During our testing we have determined the necessity of both sloshing ions and fundamental ECRH heating in establishing end plugging. In addition, we found that ICRF successfully heated the central cell ions to an average energy of 1.5 keV. Our measurements of the axial potential profile have directly verified the thermal barrier potential dip and ion-confining outer potential peak characteristic of a thermal barrier end cell.

The axial ion confinement time increased an order of magnitude during end plugging--from 5 to 20 ms to 50 to 100 ms. The radial ion confinement time is approximately 100 ms for moderate central cell potentials (below that required to produce resonance between the axial bounce and E x B azimuthal drift of ions) and drops to 5 to 15 ms when potentials reach extreme values (many times the central cell temperature). The radial transport is independent of end plugging. Finally, a two-fold increase in radial confinement time has been obtained by using electrically floating end plates to reduce the magnitude of the central cell potential above ground. These recent experimental data suggest that higher central cell densities can be reached by increasing the energy of passing ions from the central cell. Future experiments with additional ICRF heating, more efficient neutral beam injection heating, and

improved vacuum conditions in the central cell will be directed toward increasing n_c to the range of 10^{13} cm^{-3}.

REFERENCES

1. T. C. Simonen, S. L. Allen, T. A. Casper, J. F. Clauser, C. A. Clower, et al, Phys. Rev. Lett., 50, 1668, 1983.
2. T. C. Simonen, S. L. Allen, T. A. Casper, J. F. Clauser, C. A. Clower, et al, Proc. of Course/Workshop on Mirror-Based Approaches to Magnetic Fusion, Varenna, Italy, Sept. 7-17, 1983.
3. D. P. Grubb, S. L. Allen, T. A. Casper, J. F. Clauser, F. H. Coensgen, et al, "Thermal Barrier Production and Identification in a Tandem Mirror", UCRL-90536. Accepted for publication in Physical Review Letters.
4. B. W. Stallard, W. F. Cummins, A. W. Molvik, P. Poulsen, T. C. Simonen, S. Falabella, J. D. Barter, T. Christensen, G. Dimonte and T. E. Romesser, Proc. of 4th International Symposium on Heating in Toroidal Plasmas, Rome, Italy, March 21-28, 1984.
5. A. W. Molvik, W. F. Cummins, S. Falabella, P. Poulsen, J. D. Barter, G. Dimonte, T. E. Romesser, R. Mett, Proc. of 4th International Symposium on Heating in Toroidal Plasmas, Rome, Italy, March 21-28, 1984.
6. E. B. Hooper, Jr., D. E. Baldwin, T. K. Fowler, R. J. Kane, and W. C. Turner, "Radial Transport Reduction in Tandem Mirrors Using End Wall Boundary Conditions", UCRL-90639. Accepted for publication in Physics of Fluids.
7. F. H. Coensgen, T. C. Simonen, A. K. Chargin and B. G. Logan, TMX-U Proposal, LLL-PROP-172.
8. R. H. Cohen, Phys. Fluids, 26, 2774, 1983.
9. Y. Matsuda, T. D. Rognlien, Phys. Fluids, 26, 2778, 1983.
10. A. W. Molvik, S. Falabella, "Use of ICRH for Startup and Initial Heating of the TMX-U Central Cell", UCID-19342, 1982.
11. S. L. Allen, T. L. Yu, T. J. Nash, "Impurity Characteristics in TMX-U," UCID-20026, May 1984.
12. T. J. Orzechowski, S. L. Allen, J. H. Foote, R. K. Goodman, A. W. Molvik, T. C. Simonen, Phys. Fluids 26, 2335, 1983.
13. T. A. Casper, G. Smith, Phys. Rev. Lett., 48, 1015, 1982.
14. W. C. Turner, E. J. Powers, T. C. Simonen, Phys. Rev. Lett., 39, 1087, 1977.
15. B. W. Stallard, W. Nevins, Y. Matsuda, Nucl. Fusion, 23, 213, 1983.
16. C. J. Lasnier, R. A. James, R. F. Ellis, Bull. Am. Phys. Soc., 28, 1117, 1983.

17. T. A. Casper, L. V. Berzins, R. F. Ellis, R. A. James, C. Lasnier, "Microstability of TMX-U During Initial Thermal Barrier Operation" UCRL-90451, submitted to International Conference on Plasma Physics, Lausanne, Switzerland, 1984. Also T. A. Casper, Y.-J. Chen, R. Ellis, R. James, C. Lasnier, "Initial Assessment of Hot Electron Microstability in the Initial TMX-U Experiments," UCID-19783.

18. Y.-J. Chen, W. M. Nevins, G. R. Smith, Proc. of the 2nd Workshop: Hot Electron Ring Physics, 1981 (San Diego, CA, 1981) Vol. 2, p. 279.

19. Y. Y. Lau, K. R. Chu, Phys. Rev. Lett. 50, 243 (1983).

20. M. Porkolab, Phys. Fluids 27, 162 (1984).

21. A. W. Molvik, Rev. Sci. Inst. 52, 704 (1981).

22. R. K. Goodman, T. D. Rognlien, "Initial Simultaneous Thomson Scattering Measurements in the TMX-U Tandem Mirror", UCID-19943, 1983.

23. W. C. Turner, W. E. Nexsen, S. L. Allen, E. B. Hooper, A. L. Hunt, et al, "Gas Pressure in the End Plug Regions of the TMX-U Thermal Barrier Experiment", UCRL-89938, Dec. 1983, to be published.

24. D. E. Baldwin, R. H. Cohen, T. B. Kaiser, B. G. Logan, L. D. Pearlstein, M. Porkolab, M. E. Rensink, Proc. of 8th Intl. Conf. on Plasma Physics and Conf. Fusion Research, IAEA, Brussels, 1980, vol. 1, pg. 133.

25. A. A. Mirin, S. P. Auerbach, R. H. Cohen, J. M. Gilmore, L. D. Pearlstein, M. E. Rensink, Nucl. Fusion 23, 703 (1983).

26. R. H. Cohen, Radial Transport Workshop, Monterey, June 11-12, 1984 and private communication.

FIGURE CAPTIONS

Fig. 1. Magnet and heating systems for TMX-U.

Fig. 2. Axial profiles of magnetic field strength and potential (top), electron density (center), and ion density (bottom) in the end plugs.

Fig. 3. Diagnostic signals in the east plug, central cell, and west plug, which illustrate startup of end plugging in TMX-U.

Fig. 4. Sloshing-ion angular distribution (a) and axial density distribution (b).

Fig. 5. Hot electron data showing (a) buildup of diamagnetism vs time, (b) average hot electron beta vs ECRH energy input, and (c) hot electron density vs total electron density for shots with and without end plugging.

Fig. 6. Spatial profiles of hot electrons that determine a 20-cm parabolic radius and a 64-cm Gaussian half length: (a) radial profile of diamagnetism vs limiter radius, (b) radiometer emission vs limiter radius, and (c) diamagnetism and radiometer emission vs axial position.

Fig. 7. Measurement of the axial potential profile in the thermal barrier: (a) profile of the magnetic field with illustration of the heating systems used for single-end plugging operation and (b) potential vs axial position.

Fig. 8. Initial Thomson-scattering measurements: (a) central cell electron temperature T_{ec} vs electron temperature T_{ep} at the outer potential peak, (b) scattered intensity vs wavelength squared, showing the non-Maxwellian character of electrons in the outer potential peak, and (c) results of a Monte Carlo calculation of the non-Maxwellian electron distribution in the outer potential peak.

Fig. 9. Diagnostic signals measured during ICRF heating: (a) plasma density, (b) ICRF power, (c) mean perpendicular temperature of the central cell ions, and (d) average energy of ions lost axially.

Fig. 10. Increase in central cell density as a function of recent machine improvements.

Fig. 11. Central cell density vs temperature of the required passing ions for end-plugging operations.

Fig. 12. Scaling of nonambipolar radial ion transport for $r \leq 12.9$ cm with central cell potential ϕ_e.

Fig. 13. Plasma behavior with electrically floating end plates: (a) schematic of the end plates, (b) central cell line density vs time (t) with the end plates initially floating and then shorted at t = 35 ms, and (c) ratio (R) of line densities measured on radial chords through r = 0 and r = 13 cm.

W. C. Turner et al. - Figure 1

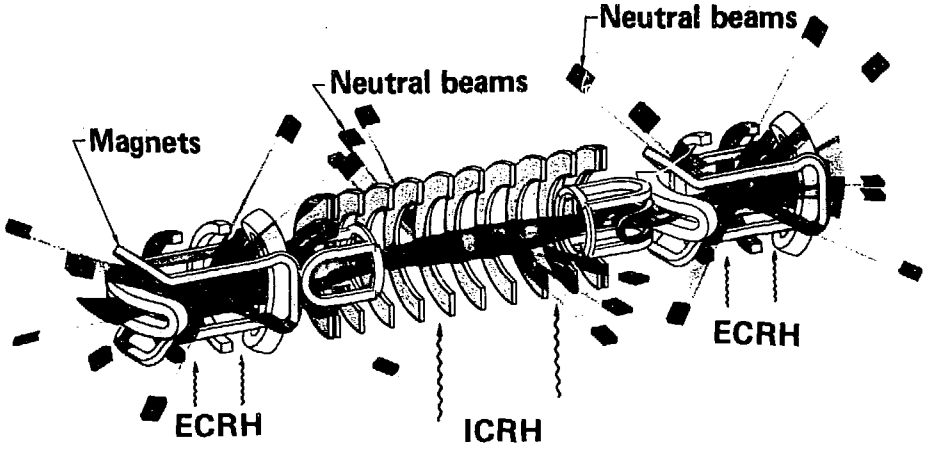

W. C. Turner et al. - Figure 2

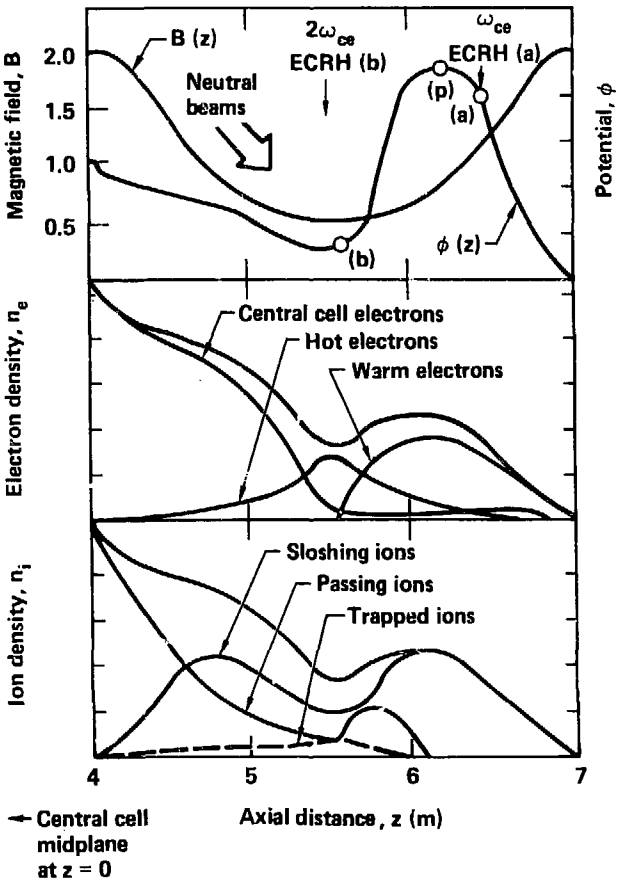

W. C. Turner et al. - Figure 3

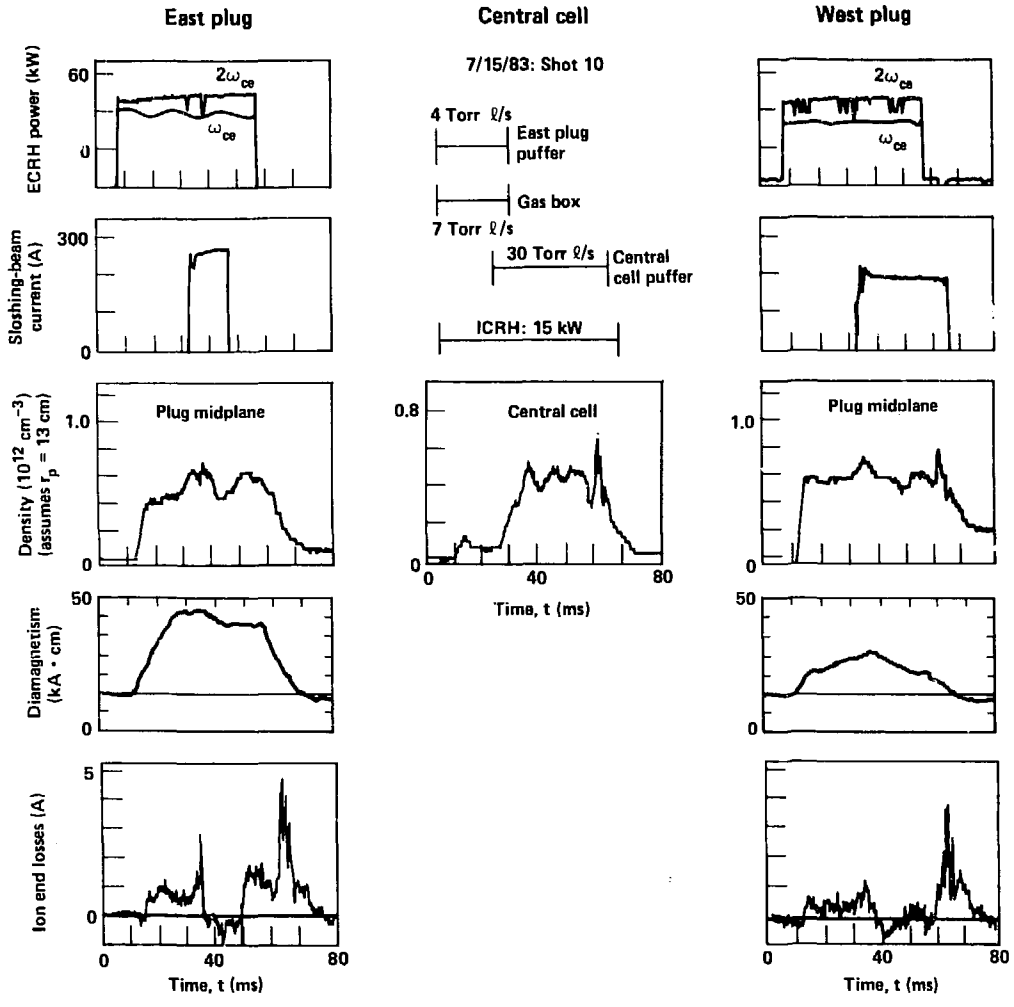

W. C. Turner et al. - Figure 4

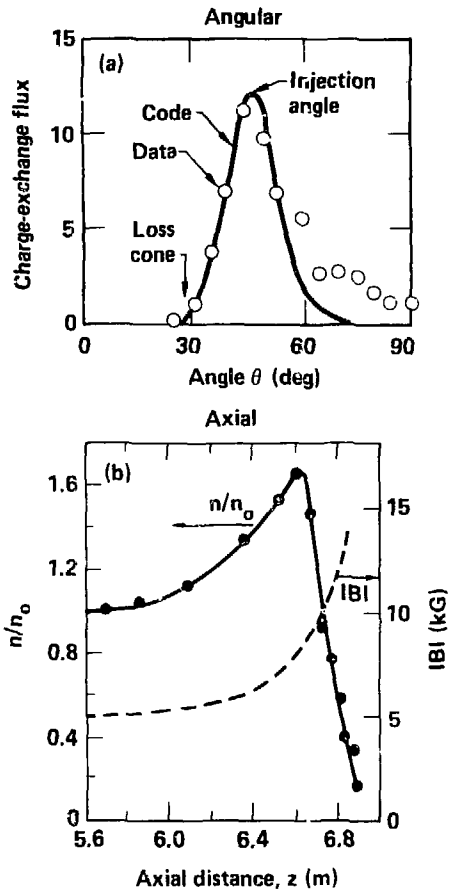

W. C. Turner et al. - Figure 5

(a) Diamagnetism buildup

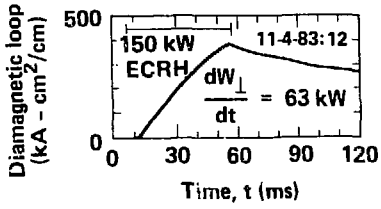

(b) Average beta

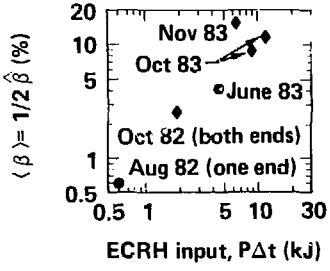

(c) Hot electron density required for plugging

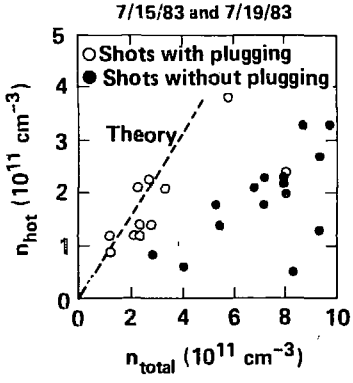

W. C. Turner et al. - Figure 6

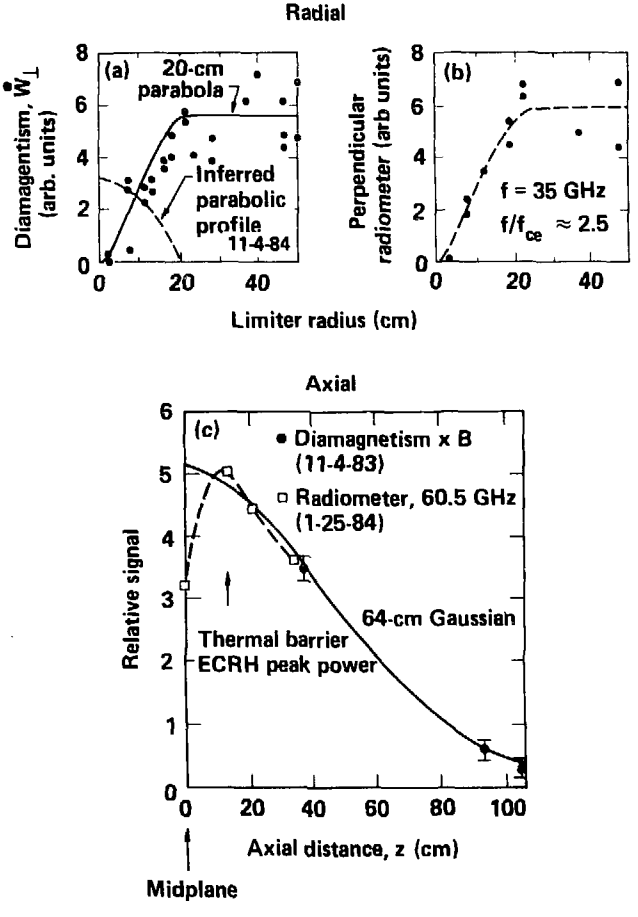

W. C. Turner et al. - Figure 7

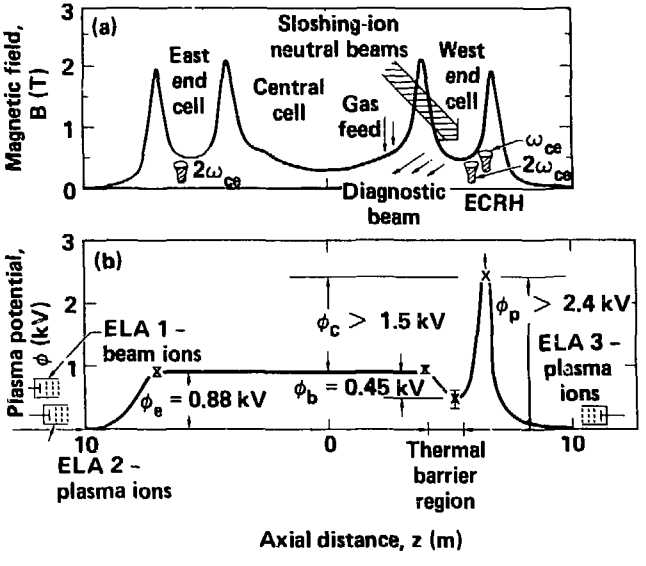

W. C. Turner et al. - Figure 8

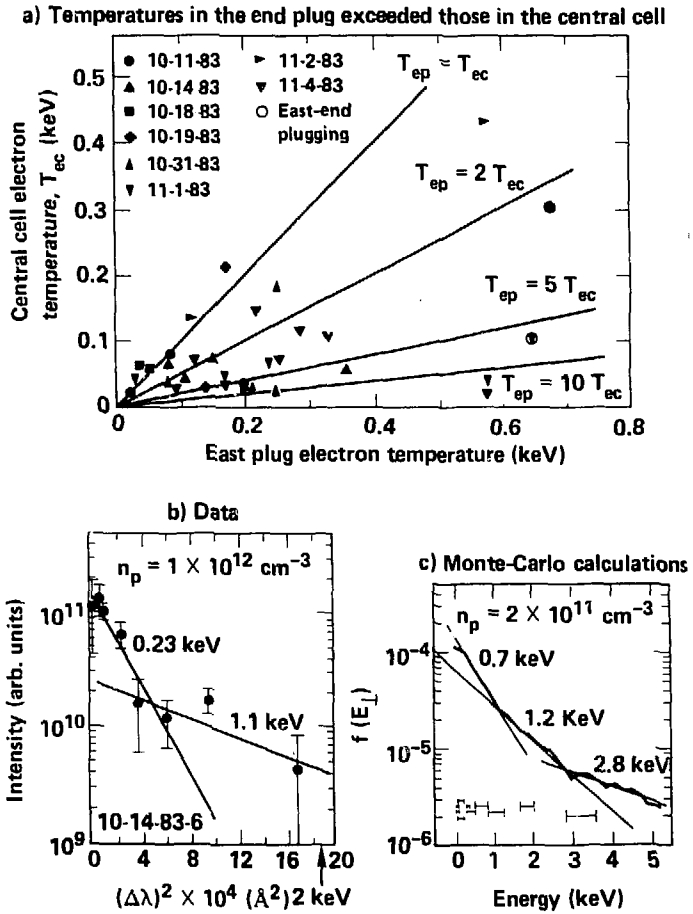

W. C. Turner et al. - Figure 9

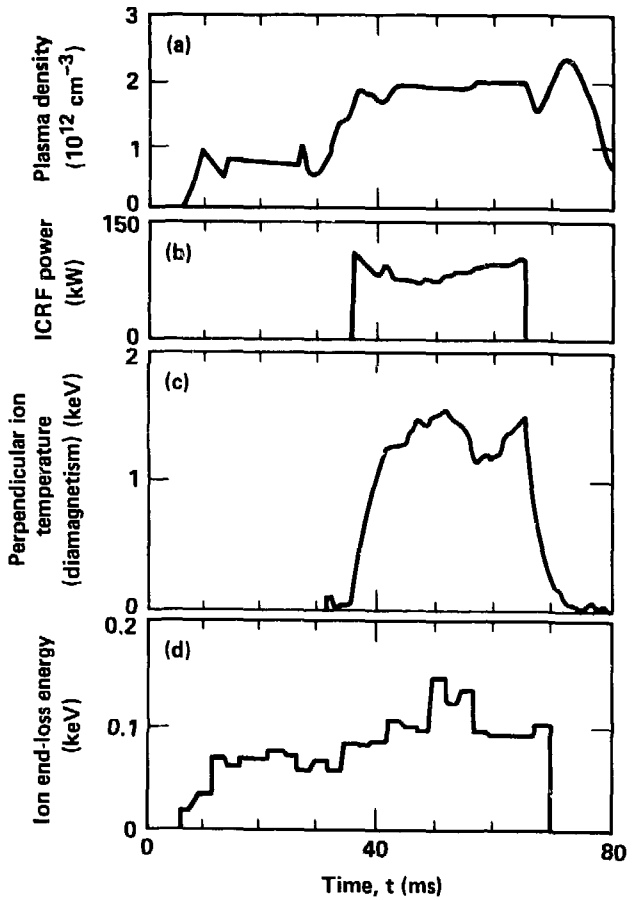

W. C. Turner et al. - Figure 10

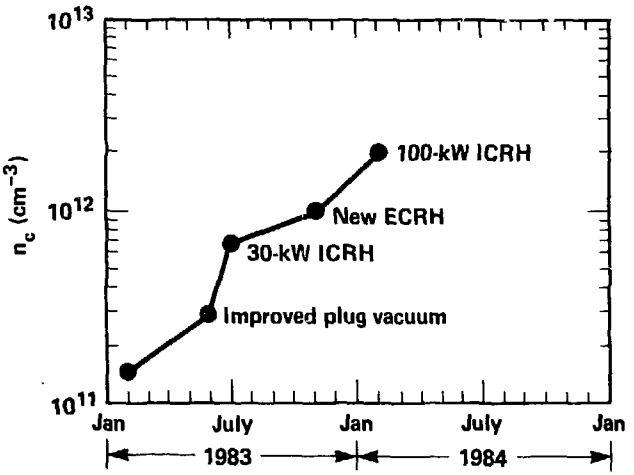

W. C. Turner et al. - Figure 11

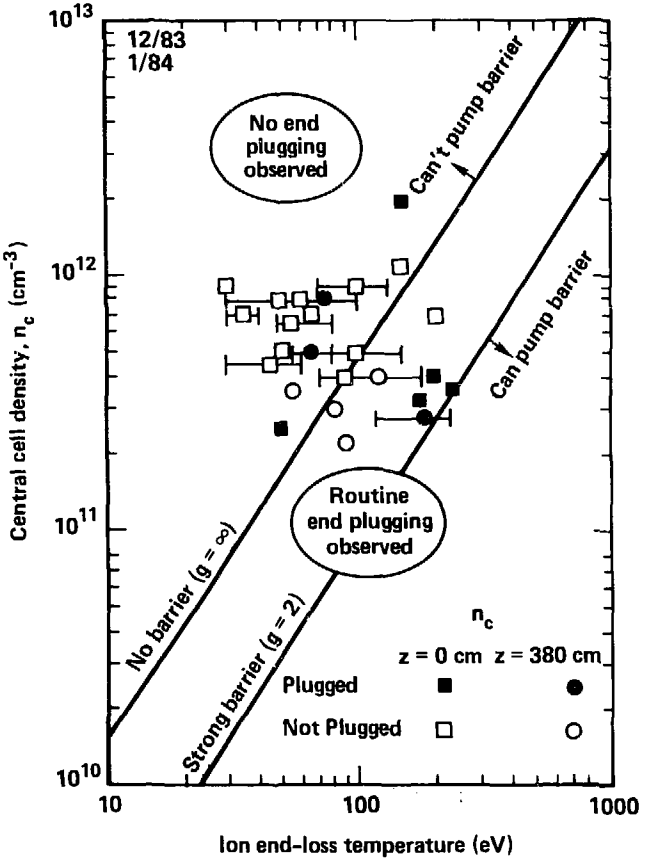

W. C. Turner et al. - Figure 12

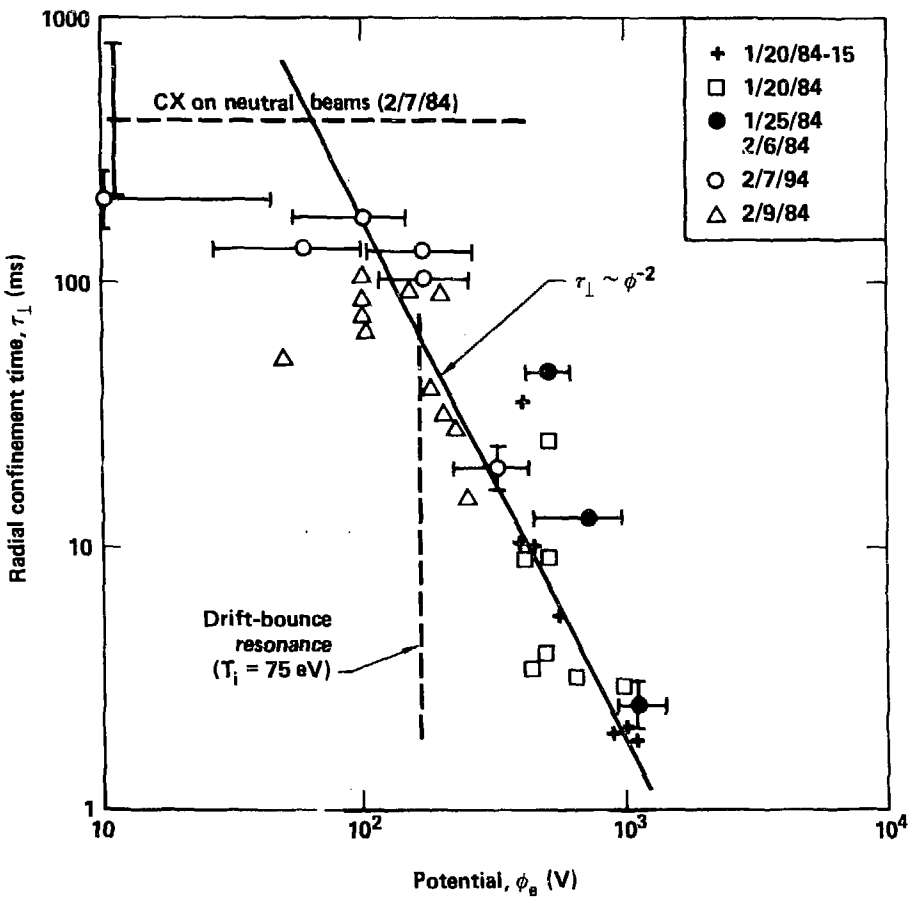

W. C. Turner et al. - Figure 13

(a) Schematic of end wall plates

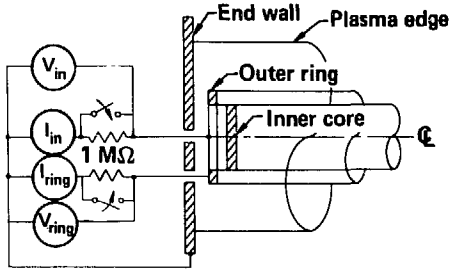

(b) On-axis line density

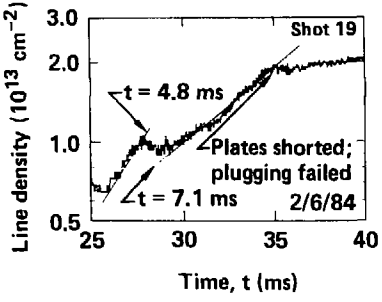

(c) Ratio of on-axis to off-axis (13-cm) line density